



Small waterbodies reduce the carbon sink of a polygonal tundra landscape

Lutz Beckebanze^{1,2,*}, Zoé Rehder^{3,4,*}, David Holl^{1,2}, Charlotta Mirbach^{1,2}, Christian Wille⁵, and Lars Kutzbach^{1,2}

¹Institute of Soil Science, Universität Hamburg, Germany

²Center for Earth System Research and Sustainability (CEN), Universität Hamburg, Germany

³Department of the Land in the Earth System, Max Planck Institute for Meteorology, Hamburg, Germany

⁴International Max Planck Research School on Earth System Modeling, Hamburg, Germany

⁵Helmholtz-Zentrum Potsdam – Deutsches Geo Forschungs Zentrum (GFZ), Potsdam, Germany

*These authors contributed equally to this work.

Correspondence: Lutz Beckebanze (lutz.beckebanze@uni-hamburg.de), Zoé Rehder (zoe.rehder@mpimet.mpg.de)

Abstract. Arctic permafrost landscapes have functioned as a global carbon sink for millennia. These landscapes are very heterogeneous, and the omnipresent waterbodies are a carbon source within them. Yet, only a few studies focus on the impact of these waterbodies on the landscape carbon budget. We compare carbon dioxide and methane fluxes from small waterbodies to fluxes from the surrounding tundra using eddy covariance measurements from a tower located between a large pond and semi-terrestrial vegetated tundra.

When taking the open-water areas of small waterbodies into account, the carbon dioxide sink strength of the landscape was reduced by 11%. While open-water methane emissions were similar to the tundra emissions, some parts of the studied pond's shoreline exhibited much higher emissions, underlining the high spatial variability of methane emissions. We conclude that gas fluxes from small waterbodies can contribute significantly to the carbon budget of arctic tundra landscapes. Consequently, changes in arctic hydrology and the concomitant changes in the waterbody distribution may substantially impact the overall carbon budget of the Arctic.

1 Introduction

Waterbodies make up a significant part of the arctic lowlands with an areal coverage of about 17%, (Muster et al., 2017) and considerably decrease the landscape carbon sink (Kuhn et al., 2018). The thaw of permafrost in the warming Arctic is going to change the distribution of waterbodies (Andresen and Lougheed, 2015; Bring et al., 2016) and thus also their contribution to the landscape-carbon budget (Kuhn et al., 2018). However, data on greenhouse-gas emission from arctic waterbodies are still sparse in space and time, especially with a high temporal resolution and in non-Yedoma regions (Vonk et al., 2015).

Our study site, in the Lena River Delta, Siberia, is located on an island mostly covered by non-Yedoma polygonal tundra (Fig. 1). This landscape features many ponds (defined here by an area $< 8 \cdot 10^4$ m², Ramsar Convention Secretariat (2016); Rehder et al. (2021)), as opposed to larger lakes, and in our area of interest, ponds cover about as much area as lakes (Abnizova et al., 2012; Muster et al., 2012). Ponds emit more greenhouse gases per area than lakes (Holgerson and Raymond, 2016; Wik



et al., 2016), thus, in our study area, they have a higher potential than lakes to reduce the carbon sink of the surrounding tundra (McGuire et al., 2012; Jammet et al., 2017; Kuhn et al., 2018). To estimate the impact of ponds, we compare landscape carbon dioxide (CO₂) and methane (CH₄) fluxes from the open-water area of ponds to the more commonly reported fluxes from the
25 semi-terrestrial tundra (defined here as wet and dry tundra as well as overgrown water).

Different geophysical and biochemical processes drive pond emissions of CO₂ and of CH₄. Aquatic CO₂ production is dominated by the microbial decomposition of dissolved organic carbon, which is introduced laterally into the aquatic system through rain and melt water (Neff and Asner, 2001). When supersaturated with dissolved CO₂, ponds emit CO₂ to the atmosphere through diffusion. While photosynthetic CO₂ uptake has been observed in some clear arctic waterbodies (Squires and
30 Lesack, 2003), most arctic waterbodies are net CO₂ sources (Kuhn et al., 2018). Estimates range from close to zero (0.028 g m² d⁻¹ by Treat et al. (2018), or 0.059 g m² d⁻¹ by Jammet et al. (2017)) to substantial CO₂-C emissions (1.4 – 2.2 g m² d⁻¹ by Abnizova et al. (2012)).

CH₄ emissions have been found to vary even more (by up to five orders of magnitude within just one site: 0.5 – 6432 mg m² d⁻¹, Bouchard et al. (2015)). In contrast to CO₂, most CH₄ originates in the sub-aquatic soils. It is emitted from waterbodies
35 not only through diffusion but also through ebullition (sudden release of bubbles) and plant-mediated transport, often leading to high spatial variability between waterbodies and within one waterbody (Sepulveda-Jauregui et al., 2015; Jansen et al., 2019). Local seep-ebullition events can cause high spatial variance of CH₄ emissions within one waterbody (Walter et al., 2006). Varying coverage of vascular plants in the shallow parts of a waterbody can also increase CH₄ variability through plant-mediated transport (Knoblauch et al., 2015; Andresen et al., 2017).

To study both spatial and temporal patterns, we analyze land-atmosphere CO₂ and CH₄ flux observations from an eddy covariance (EC) tower located on Samoylov Island, Lena River Delta, Russia. We set the EC tower up within the polygonal tundra next to a merged polygonal pond for two months in summer 2019. A merged polygonal pond is a larger pond which formed through the subsidence of several polygons. The polygonal structures are still clearly visible along the shore and under water, and these ponds tend to be shallow for their size (Rehder et al., 2021). Due to the tower's position, fluxes from the merged
45 polygonal pond are the dominant source of the observed EC fluxes under easterly winds. The observed EC fluxes are dominated by vegetated polygonal tundra with only a low fraction from polygonal-center ponds from the other wind directions. We (1) compare the waterbody and tundra fluxes with a focus on temporal and spatial patterns, and we (2) investigate the influence of the merged polygonal pond on the landscape carbon balance.

2 Methods

50 2.1 Study Site

The study site Samoylov Island (72°22'N, 126°28'E) is located in the southern part of the Lena River Delta (Figure 1, b). It has a size of about 5 km² and consists of two geomorphologically different parts. The western part (~2 km²) is a floodplain and regularly flooded during the annual spring flood. The eastern part (~3 km²), a late-Holocene river terrace, is characterized by polygonal tundra. The partially degraded polygonal tundra at this study site shows a high spatial heterogeneity within a



55 few meters. Dry and wet vegetated parts are interspersed with small and large ponds ($<1 \text{ m}^2 - >10000 \text{ m}^2$) and with large
thermokarst lakes (up to 0.05 km^2 , Boike et al. (2015a); Kartoziia (2019)). The island is surrounded by partially and regularly
flooded branches of the Lena River and sandy floodplains, creating more spatial heterogeneity on a larger scale. We focus on
a merged polygonal pond (Figure 1, d), which is located in the eastern part of the island. The merged polygonal pond in our
study has a size of 0.024 km^2 with a maximum depth of 3.4 meters and a mean depth of 1.2 meters (Rehder et al., 2021; Boike
60 et al., 2015a). On an aerial image, the polygonal structures are still clearly visible under the water surface (Boike et al., 2015c).
The vegetated shoreline of this merged polygonal pond is dominated by *Carex aquatilis* interspersed with *Carex chordorrhiza*,
Potentilla palustris and *Aulacomnium spp.*. Some plants grow in the water of the pond close to the shore. The deeper parts of
the pond are vegetation free.

2.2 Instruments

65 We measured gas fluxes using an eddy covariance (EC) tower between July 11 and September 10, 2019. The EC tower was
located on the eastern part of Samoylov Island, directly at the western shore of the merged polygonal pond (Figure 1, d). The EC
instruments were mounted on a tripod at the height of 2.25 meters. The tower was equipped with a closed-path $\text{CO}_2/\text{H}_2\text{O}$ sensor
(LI-7200, LI-COR Biosciences, USA), an open-path CH_4 sensor (LI-7700, LI-COR Biosciences, USA), and a 3D-ultrasonic
anemometer (R3-50, Gill Instruments Limited, UK). All instruments had a sampling rate of 20 Hz.

70 Additional meteorological data for Samoylov Island was provided by Boike et al. (2019). We also installed radiation-shielded
temperature and humidity sensors at the EC tower (HMP 155, Vaisala, Finland) and used data from a photosynthetically active
radiation (PAR) sensor mounted at a tower approximately 500 meters to the west (SKP 215, Skye Instruments, UK).

2.3 Data Processing

We perform the raw data processing and computation of half-hourly fluxes for open-path and closed-path fluxes using *EddyPro*
75 *7.0.6* (LI-COR, 2019). Raw data screening includes spike detection and removal according to Vickers and Mahrt (1997) (1%
maximum accepted spikes and a maximum of 3 consecutive outliers). Additionally, we apply statistical tests for raw data
screening, including tests for amplitude resolution, skewness and kurtosis, discontinuities, angle of attack, and horizontal winds
steadiness. All parameters of these tests are set to *EddyPro* default values. We rotate the wind-speed axis to a zero-mean vertical
wind speed using the "double rotation"-method by Kaimal and Finnigan (1994). We apply linear de-trending following Gash
and Culf (1996) to the raw data prior to the flux calculation. We compensate time lags by automatic time-lag optimization using
80 a time-lag-assessment file from a previous *EddyPro* run. In this previous time-lag assessment, the time lags for all gases are
detected by covariance maximization (Fan et al., 1990) resulting in time lags of $0 - 0.4 \text{ s}$ for CO_2 and $-0.5 - +0.5 \text{ s}$ for CH_4 . For
 H_2O , the time lag is humidity-dependent and is calculated for ten humidity classes. We compensate for air-density fluctuations
due to thermal expansion/contraction and varying water-vapor concentrations following Webb et al. (1980). This correction is
85 only applied to open-path data; for closed-path data, we perform a sample-by-sample conversion into mixing-ratios to account
for air-density fluctuations (Ibrom et al., 2007b; Burba et al., 2012). Flux losses occur in the low- and high-frequency spectral
range due to different filtering effects. In the low-frequency range, we compensate flux losses following Moncrieff et al. (2004)

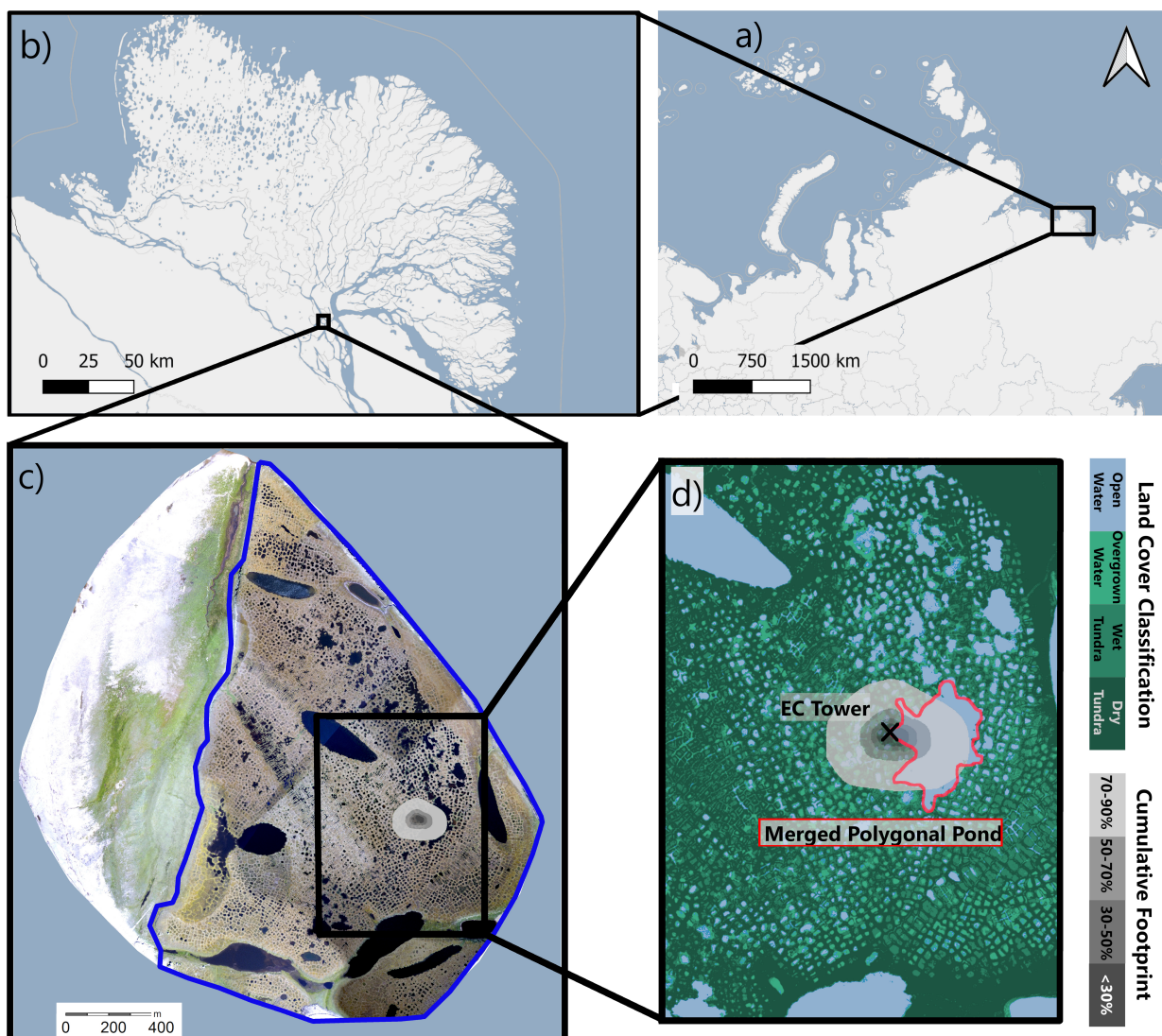


Figure 1. Study site with an overview of Russia (a), the Lena River Delta (b), Samoylov Island with the surrounding Lena River in blue (c), and a close-up look at the study site (d). The EC tower is marked as a black cross with the cumulative footprint (see section 2.4.2) in gray shades surrounding the EC tower. The outline of the land cover classification from section 2.4.1 is shown in a blue line (c). In (d), the detailed land cover classification is shown in blue (open water) and green shades (dark green: dry tundra, medium green: wet tundra, and light green: overgrown water). The merged polygonal pond studied here is outlined in red. Map data from © OpenStreetMap contributors 2020, distributed under the Open Data Commons Open Database License (ODbL) v1.0 (a & b) and modified after Boike et al. (2012) (c & d).



and in the high-frequency range following Fratini et al. (2012). For applying the latter method, a spectral assessment file is created using the method by Ibram et al. (2007a). The spectral assessment results in cut-off frequencies of 3.05 Hz and 1.67 Hz for CO₂ and CH₄, respectively. For H₂O, we find a humidity-dependent cut-off frequency between 1.25 Hz (RH 5 - 45%) and 0.21 Hz (RH 75 - 95%). We perform a quality check of each flux interval following the 0-1-2 system by Mauder and Foken (2004). In this quality check, flux intervals with the lowest quality receive the flag "2" and are excluded from further analysis.

2.4 Data Analysis

2.4.1 Land Cover Classification

The land cover classification covers the late-Holocene river terrace of Samoylov Island (Siberia, Russia). It is based on high-resolution near-infrared (NIR) orthomosaic aerial imagery obtained in the summer of 2008 (Boike et al., 2015b). We use a subset of the existing classification by Muster et al. (2012) as a training dataset to perform a semi-supervised land cover classification using the *maximum likelihood algorithm* in ArcMap Version 10.8 (ESRI Inc, USA). We then apply the ArcMap *majority filter* tool to the new classification. The land cover classification has a resolution of 0.17 m x 0.17 m, it is projected onto WGS 1984 UTM Zone 52N and the classes include *open water*, *overgrown water*, *dry tundra*, and *wet tundra*, as defined by Muster et al. (2012).

2.4.2 Footprint Model

The tower location and sensor height are crucial parameters in the deployment of an EC measurement tower. A lower measurement height results in a smaller footprint. The footprint describes the source area of the flux from the surrounding landscape. With our sensors installed at the height of 2.25 m next to the merged polygonal pond, we expect to observe substantial flux signals from the adjacent waterbody as well as from the surrounding polygonal tundra. Each land cover type's contribution to the flux signal depends on the wind direction and turbulence in the atmospheric boundary layer. We implement the analytical footprint model by Kormann and Meixner (2001) in Matlab 2019b (MATLAB, 2019) and combine the footprint model with land cover classification data described in section 2.4.1 to estimate the contribution of each land cover type to each flux signal (hereinafter referred to as the weighted footprint fraction). The model accounts for the stratification of the atmospheric boundary layer and requires a height-independent crosswind distribution and horizontal homogeneity of the surface. The input data require the stationarity of atmospheric conditions during the flux interval of 30 minutes. We derive the vertical power-law profiles for the eddy diffusivity and the wind speed for each 30-minute flux interval depending on the atmospheric stratification (equation 6 in Kormann and Meixner (2001)). We use an analytical approach to find the closest Monin-Obukhov (M-O) similarity profile (equation 36 in Kormann and Meixner (2001)). Next, we calculate a two-dimensional probability density function of the source area for each flux interval (from equation 9 and 21 in Kormann and Meixner (2001)) and combine each probability density function with the land cover classification of the river terrace of Samoylov Island, with its four land cover types (see section 2.4.1). The footprint model's resolution is set to the land cover classification resolution of 0.17 m x 0.17 m. Hence, for each grid cell within the source area, we can estimate the probability of the fraction of flux originating from this grid cell



120 for each 30-min interval. We also know the dominant land cover type in each grid cell from the land cover classification. We
combine both information for each grid cell and calculate the sum of the fraction fluxes within the source area for each of the
four land-cover types (*dry tundra*, *wet tundra*, *overgrown water* and *open water*) and obtain the contribution of each land cover
type to each 30-minute flux ($a_{dry\ tundra}$, $a_{wet\ tundra}$, $a_{overgrown\ water}$, and $a_{open\ water}$). We refer to this contribution of each
land cover type as the *weighted footprint fraction*. We combine the contributions of the *dry tundra*, *wet tundra*, and *overgrown*
125 *water* to a single land cover class for the semi-terrestrial tundra $a_{tundra} = a_{dry\ tundra} + a_{wet\ tundra} + a_{overgrown\ water}$.

We also take the sum of all 30-min two-dimensional probability density functions over the whole deployment time. This
sum is referred to as the cumulative footprint. The cumulative footprint is shown as a gray shaded area in Figure 1, c and d.
The light gray area's outer boundary represents the 90%, and the light gray area's inner boundary is the 70% isoline of the
cumulative footprint. This means that there is a probability of 10% that fluxes observed at the EC tower originate from areas
130 outside of the light gray area. Medium gray represents 50-70%, medium-dark gray 30-50%, and dark gray indicates that there
is a probability of less than 30% that the observed flux originates from within the marked area.

2.4.3 Bulk Model / Gap-Filling CO₂ Flux

We use the bulk net-ecosystem exchange of CO₂ (NEE) model by Runkle et al. (2013) to gap-fill and partition our NEE flux
observations. This model was specifically developed for modeling NEE in arctic regions taking into account the polar day. We
135 estimate all model parameters for running 5-day periods to capture changing plant physiology during the measurement period.
NEE is partitioned into two components (equation 3): total ecosystem respiration TER ($\mu\text{mol m}^{-2} \text{s}^{-1}$, equation 1) and gross
primary production GPP ($\mu\text{mol m}^{-2} \text{s}^{-1}$, equation 2). Parameters of both components are fit simultaneously. TER is modeled
as an exponential function of air temperature T_{air} :

$$\text{TER} = R_{base} \cdot Q_{10}^{\frac{T_{air} - T_{ref}}{\gamma}} \quad (1)$$

140 where $T_{ref} = 15\text{ }^{\circ}\text{C}$ and $\gamma = 10\text{ }^{\circ}\text{C}$ are constant, independent parameters. R_{base} ($\mu\text{mol m}^{-2} \text{s}^{-1}$) describes the basal respi-
ration at the reference temperature T_{ref} and Q_{10} (dimensionless) the sensitivity of ecosystem respiration to air temperature
changes.

GPP is modeled as an rectangular hyperbolic function of PAR ($\mu\text{mol m}^{-2} \text{s}^{-1}$):

$$\text{GPP} = - \frac{P_{max} \cdot \alpha \cdot \text{PAR}}{P_{max} + \alpha \cdot \text{PAR}} \quad (2)$$

145 where α ($\mu\text{mol } \mu\text{mol}^{-1}$) is the initial canopy quantum use efficiency (slope of the fitted curve at $\text{PAR} = 0$) and P_{max} ($\mu\text{mol m}^{-2} \text{s}^{-1}$)
the maximum canopy photosynthetic potential for $\text{PAR} \rightarrow \infty$.

We sum both components to estimate the modeled NEE $F_{CO_2,mod}$:

$$F_{CO_2,mod} = \text{TER} + \text{GPP}. \quad (3)$$

We split the datasets into a training (70%) and a validation (30%) data set to test model performance. Additionally, we ex-
150 clude CO₂ fluxes from the direction of the merged polygonal pond from the training dataset to obtain a dataset consisting of as



much semi-terrestrial tundra as possible since we do not expect photosynthetic activity in the non-overgrown merged polygonal pond.

We implement the bulk model in Matlab 2019b (MATLAB, 2019) using the *fit* function with the fit-method of *NonLinear-LeastSquares*. We use the *coeffvalues*-function to estimate the four parameters and the *confint*-function to estimate their 95% confidence bounds. All partitioned fluxes are converted into CO₂-C fluxes in the unit g m⁻² d⁻¹ prior to the data analysis.

2.4.4 Aquatic CO₂ Flux

In a heterogeneous landscape, fluxes observed using the EC method contain information from different land cover types. In this study, we extract fluxes primarily related to ponds and tundra from the mixed signals. We then combine these estimated fluxes to analyze the influence of ponds on a polygonal tundra landscape.

To estimate the CO₂ flux from the merged polygonal pond (F_{pond}), we first fit a bulk model to data from which we exclude fluxes from the merged polygonal pond (thus exclude fluxes >30° & >150° wind direction). This modeled CO₂ flux ($F_{modeled,mix}$) represents the vegetated tundra surrounding the EC tower, including small ponds to the north, west and south (with a weighted footprint fraction of open water of <30% in each flux signal). In a second step, we make the assumption that individual contributions from different land cover types to the observed flux scale linearly with their contribution to the footprint. Thus, we can calculate the observed CO₂ flux ($F_{obs,mix}$) as the sum of the individual land cover type fluxes ($F_{modeled,mix}$ and F_{pond}) each multiplied with their weighted footprint fraction a_{tundra} and a_{pond} , respectively, where $a_{open\ water} = a_{pond}$, $a_{tundra} = a_{sum} - a_{pond}$, and a_{sum} being the sum over all land cover classes:

$$\begin{aligned} F_{obs,mix} &= a_{pond} \cdot F_{pond} + a_{tundra} \cdot F_{modeled,mix} \\ \Leftrightarrow F_{pond} &= \frac{F_{obs,mix} - a_{tundra} \cdot F_{modeled,mix}}{a_{pond}} \end{aligned} \quad (4)$$

To improve data quality, we exclude 30-min flux intervals of F_{pond} when $a_{pond} < 50\%$. Then, we use the median of F_{pond} for further calculations.

As mentioned above, the observed CO₂ flux from the north, west, and south ($F_{obs,mix}$) is still influenced by small ponds. To analyze in detail the CO₂ flux from the vegetated tundra ($F_{modeled,veg}$), we subtract the previously estimated pond-CO₂ flux F_{pond} from the observed CO₂ flux $F_{obs,mix}$:

$$F_{modeled,veg} = \frac{F_{obs,mix} - a_{pond} \cdot F_{pond}}{a_{tundra}} \quad (5)$$

We then use this estimated CO₂ flux from the vegetated tundra $F_{modeled,veg}$ as the input variable for the bulk model to receive a gap-filled dataset of CO₂ flux from vegetated tundra.



2.4.5 Up-scaled CO₂ flux

180 To evaluate the impact of ponds on landscape CO₂ flux without the influence of ponds, we estimate a polygonal-tundra landscape-CO₂ flux ($F_{Landscape}$) including ponds by linearly combining the two landscape forms (ponds and vegetated tundra):

$$F_{Landscape} = A_{pond} \cdot F_{pond} + A_{tundra} \cdot F_{tundra}$$

where F_{pond} describes the CO₂ emission from the merged polygonal pond (equation 4), F_{tundra} the modeled CO₂ flux from the vegetated tundra (equation 5), $A_{pond} = 0.07$ the coverage of open pond water on the whole river terrace of Samoylov Island (from the land cover classification, section 2.4.1) and $A_{tundra} = 1 - 0.07$ the coverage of other land cover types. We do not account for (larger, deeper) thermokarst lakes in this up-scaling approach, as we expect different greenhouse gas processes from these lakes and there are no lakes in our footprint. Thus, we scale the above numbers to $A_{tundra} + A_{pond} = 1$ which results in $A_{pond} = 0.076$ and $A_{tundra} = 0.924$.

3 Results

190 3.1 Meteorological Conditions

During the measurement period between 11 July and 10 September 2019, half-hourly air temperatures ranged from -0.5 °C to 27.6 °C with a mean temperature of 8.7 °C (Figure A1, a). The maximum wind speed measured on the EC tower at 2.25 m height was 8.9 m s⁻¹ (Figure A1, b). Photosynthetically active radiation (PAR) reached values of up to 1419 μmol m⁻² s⁻¹ with decreasing maximum values during the measurement period (Figure A1, c). 28 cloudy days are clearly visible as days with low PAR-values (below ~500 μmol m⁻² s⁻¹) throughout the measurement period.

3.2 CO₂ Fluxes

Figure 2 shows the observed CO₂ fluxes plotted against the wind direction. The CO₂ flux exhibits a high temporal variability between positive and negative CO₂ fluxes from most wind directions. In the wind direction sector between 60° – 120°, the flux is dominated by the merged polygonal pond. The flux signal from this sector has a smaller variability (standard deviation of 0.073 g m⁻² d⁻¹) than the fluxes from the other wind direction sectors (standard deviation of 0.56 g m⁻² d⁻¹). Additionally, we observe a lower respiration rate from the pond than from the semi-terrestrial tundra. Figure 3 shows the observed CO₂ fluxes plotted against the weighted footprint fraction of open-water in each flux when only considering night-time fluxes (PAR < 20 μmol m⁻² s⁻¹, thus only respiration). The fluxes decrease with an increasing open-water contribution. Another part of the CO₂ variability stems from the diurnal cycle. We compare the diurnal cycle of the CO₂ fluxes from the merged polygonal pond (estimated following equation 4) and the semi-terrestrial tundra (equation 5) in Figure 4. We see a less pronounced diurnal CO₂ cycle from the direction of the merged polygonal pond (blue) compared to the diurnal CO₂ cycle from the tundra (green). All data from the merged polygonal pond combined result in a CO₂-C flux of **0.13** $\frac{0.24}{0.00}$ g m⁻² d⁻¹ (Median $\frac{75\% \text{ Percentile}}{25\% \text{ Percentile}}$).

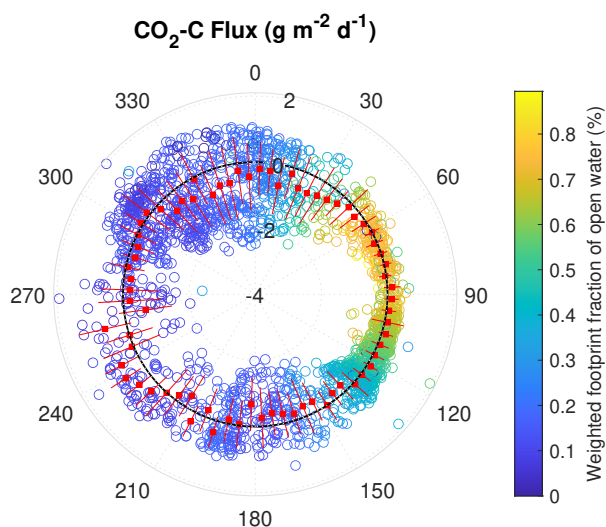


Figure 2. Polar plot of CO₂-C flux with respect to the wind direction at the EC tower. Negative values (inside of the dotted black line) represent CO₂ uptake, positive values (outside of the dotted black line) CO₂ emission. The values -4, -2, 0, and 2 indicate the magnitude of the CO₂-C flux in g m⁻² d⁻¹. The color represents the percentage of open water weighted footprint fraction in each flux interval. The red boxes indicate the mean CO₂ flux of 5° wind direction intervals (red lines indicate the first standard deviation).

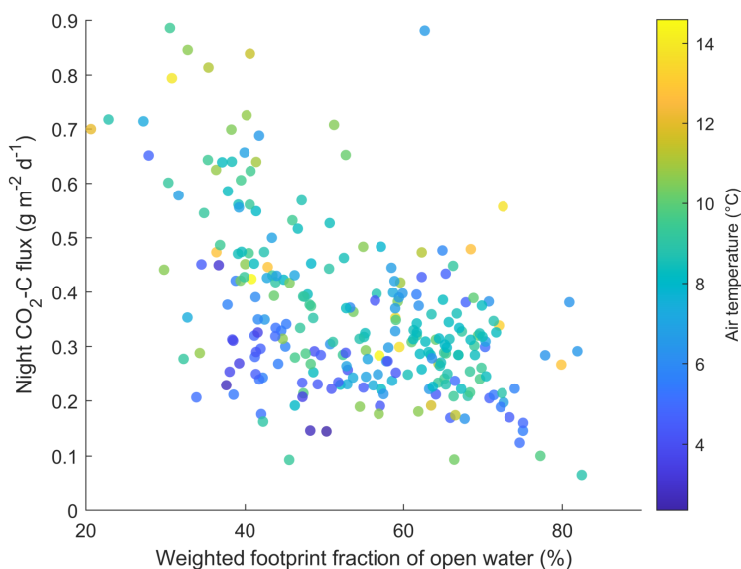


Figure 3. Scatter plot of observed CO₂ fluxes against the weighted footprint fraction of open water in each flux interval with temperature as color. Only flux intervals at night time (PAR < 20 μmol m⁻² s⁻¹) are shown.

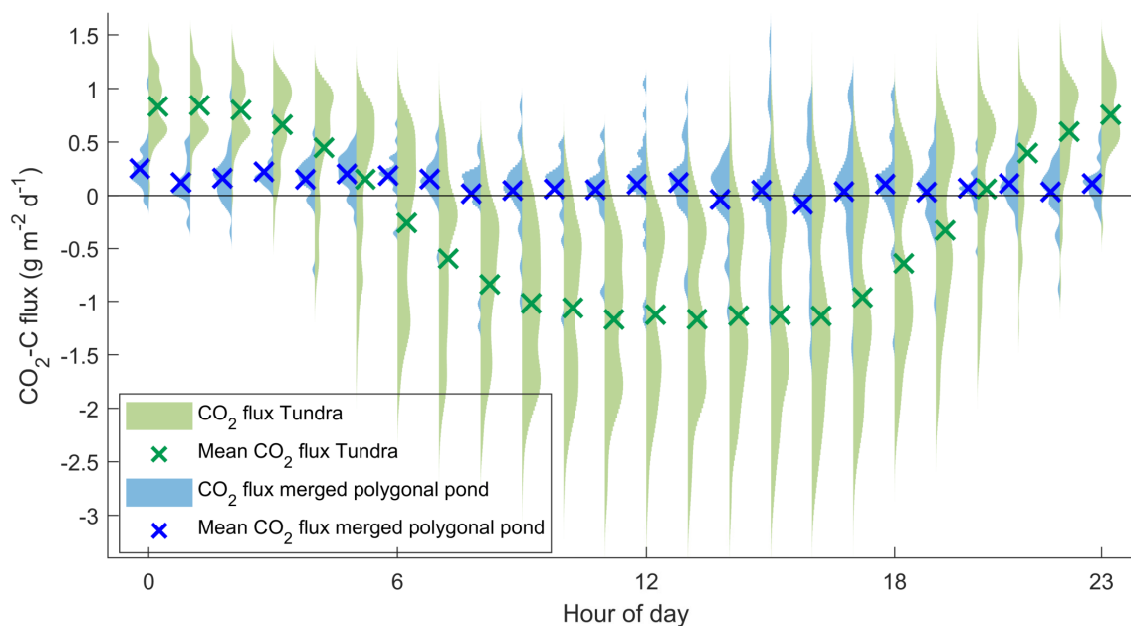


Figure 4. Diurnal cycle of modeled $\text{CO}_2\text{-C}$ flux from the merged polygonal pond (blue, eq. 4) and the tundra (green, eq. 5) as violin plots for each half-hour flux interval. Blue and green crosses mark the mean $\text{CO}_2\text{-C}$ flux during each half-hour flux interval.

3.3 CH_4 Fluxes

Figure 5 shows the observed CH_4 fluxes plotted against the wind direction. The CH_4 emissions peak at $\sim 120^\circ$, where fluxes from a shoreline of the merged polygonal pond contribute to the observed flux (see Figure 1 d, hereinafter $Shore_{120^\circ}$). We do not observe a similar peak of CH_4 emissions in the direction of the second shoreline towards $\sim 50^\circ$ ($Shore_{50^\circ}$). These peaks did not correlate with any of the four weighted footprint fractions.

To further investigate the peak at $Shore_{120^\circ}$ we separate the CH_4 emissions into four sectors depending on wind direction ($Shore_{120^\circ}$, $Shore_{50^\circ}$, *pond* and *tundra*, see Figure 6). We find the following fluxes from the wind direction sectors: $19.18 \frac{24.47}{14.26} \text{ mg m}^{-2} \text{ d}^{-1}$ ($Shore_{120^\circ}$), $12.96 \frac{15.11}{10.34} \text{ mg m}^{-2} \text{ d}^{-1}$ ($Shore_{50^\circ}$), $13.38 \frac{15.92}{10.55} \text{ mg m}^{-2} \text{ d}^{-1}$ (*pond*), and $12.55 \frac{16.07}{9.65} \text{ mg m}^{-2} \text{ d}^{-1}$ (*tundra*, *Median* $\frac{75\% \text{Percentile}}{25\% \text{Percentile}}$). Fluxes from $Shore_{120^\circ}$ have a higher median than fluxes from the other three wind sectors (see Figure 6). High wind speeds enhance turbulent mixing of the water column and diffusive CH_4 outgassing at the water-atmosphere interphase. High wind speeds are also associated with stronger pressure pumping potentially fostering ebullition, and thereby CH_4 emission. Additionally, peak temperatures can also lead to peak CH_4 production and emissions. So, we investigated these confounding factors by excluding flux intervals with high wind speed (larger than $5 \frac{\text{m}}{\text{s}}$) and high air temperature (larger than 12°C).



To evaluate whether the differences in medians between the four wind sectors are significant, we apply a permutation test (Edgington and Onghena (2007), Figure A2 and A3). In this test, we randomly assign each 30-min flux signal to one of two groups, calculate the median of both groups and their difference. After repeating this step 10000 times, we plot the resulting differences in medians in a histogram and perform a one-sample t-test to evaluate whether the observed difference in medians differs significantly ($p < 0.01$) from the randomly generated differences. In the randomization test we find evidence for a significant difference between the CH_4 emission from $Shore_{120^\circ}$ and the other three classes at low wind speeds (top row in Figure A2) and no significant difference between the CH_4 emission from the other three classes ($Shore_{50^\circ}$, *pond* and *tundra*). The results are very similar for moderate temperatures: We find evidence for a significant difference between the CH_4 emission from $Shore_{120^\circ}$ and the other three classes (top row in Figure A3). The differences in medians between the pond and $Shore_{50^\circ}$ as well as between the pond and the tundra are significant. However, this difference is much smaller (second row in Figure A3).

In summary, we find no meteorological parameter acting as a driver for the high CH_4 emission from $Shore_{120^\circ}$. Note that the CH_4 emissions from the pond and the tundra have a similar magnitude under moderate wind speed conditions. When comparing the ratio of CH_4 emissions to CO_2 emissions, we find that fluxes with an open-water weighted footprint fraction of more than 60% have a ratio of $\text{CH}_4/\text{CO}_2 = 0.057^{0.104}_{-0.049}$ (Median^{75% Percentile}_{25% Percentile}), while for fluxes intervals with less than 20% open-water contribution we observe a negative ratio (due to the negative CO_2 fluxes) with a larger spread of $\text{CH}_4/\text{CO}_2 = -0.010^{0.021}_{-0.028}$ (Median^{75% Percentile}_{25% Percentile}). The distributions of these two ratios are significantly different (Mann-Whitney-U test, $p < 0.01$). When considering only night-time fluxes ($\text{PAR} < 20 \mu\text{mol m}^{-2} \text{ s}^{-1}$), the ratio of fluxes with an open-water weighted footprint fraction of more than 60% is similar ($\text{CH}_4/\text{CO}_2 = 0.060^{0.076}_{0.049}$, Median^{75% Percentile}_{25% Percentile}), whereas ratio with less than 20% open-water contribution is now positive ($\text{CH}_4/\text{CO}_2 = 0.020^{0.024}_{0.015}$, Median^{75% Percentile}_{25% Percentile}). The distributions of these two ratios are still significantly different (Mann-Whitney-U test, $p < 0.01$).

3.4 Upscaled CO_2 flux

We use the estimated aquatic CO_2 flux from the merged polygonal pond and the modeled CO_2 flux from the semi-terrestrial tundra to linearly up-scale the CO_2 flux for the polygonal-tundra landscape of Samoylov Island (excluding larger thermokarst lakes, method described in section 2.4.5).

We estimate that the tundra CO_2 uptake would decrease by $\sim 11\%$ when including the CO_2 flux from ponds compared to a completely semi-terrestrial tundra. The modeled CO_2 -C flux from the semi-terrestrial tundra (without consideration of pond fluxes) accumulated to $-16.29 \pm 0.43 \text{ g m}^{-2}$ during the observation period (60.5 days). Separated into months, it amounts to -15.01 ± 0.26 , -3.56 ± 0.33 and $+2.35 \pm 0.11 \text{ g m}^{-2}$ in July (19.8 days), August (31 days), and September (9.7 days), respectively. When including the CO_2 flux from the merged polygonal pond as representative for all ponds on Samoylov island, the resulting estimate of the landscape CO_2 flux amounts to $-14.47 \pm 0.40 \text{ g m}^{-2}$ (60.5 days) and to monthly fluxes of -13.75 ± 0.24 , -2.99 ± 0.31 , and $+2.27 \pm 0.10 \text{ g m}^{-2}$ in July (19.8 days), August (31 days), and September (9.7 days), respectively. Thus, in August, the estimate of CO_2 uptake is reduced most. In September, the estimate of landscape emissions is decreased

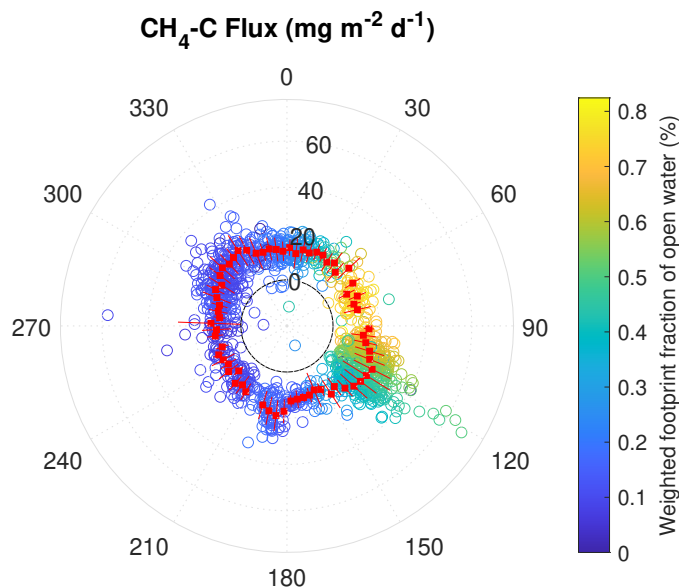


Figure 5. Polar plot of $\text{CH}_4\text{-C}$ flux with respect to the wind direction at the EC tower. Positive values outside of the dotted black line represent CH_4 emission, and inside of the line, CH_4 uptake during one half-hour period. The values 0, 20, 40, and 60 indicate the magnitude of the $\text{CH}_4\text{-C}$ flux in $\text{mg m}^{-2} \text{d}^{-1}$. The color represents the percentage of open water weighted footprint fraction in each flux interval. The red boxes indicate the mean CH_4 flux of 5° wind direction intervals (red lines indicate the first standard deviation).

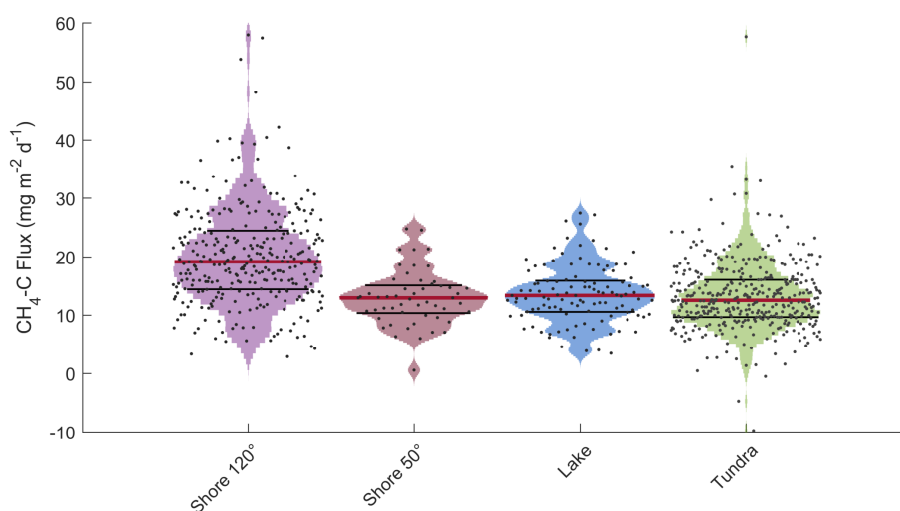


Figure 6. Violin plots of CH_4 emissions at the EC tower separated into four different wind direction classes. Medians of CH_4 emission distributions are shown as red lines, and 75th & 25th percentile are shown as black lines.



255 by 3.5% when including pond CO₂ emissions.

4 Discussion

4.1 CO₂ flux

Only a limited number of EC CO₂-flux studies from permafrost-affected ponds and lakes are available (studies with "EC" in
260 table 1). Estimates of aquatic EC CO₂-C flux range from 0.059 g m⁻² d⁻¹ (Jammet et al., 2017) over 0.11 g m⁻² d⁻¹ (Eugster
et al., 2003) to 0.22 g m⁻² d⁻¹ (Jonsson et al., 2008). Our estimate of 0.12^{0.24}_{0.0014} g m⁻² d⁻¹ is therefore well within the
range of aquatic CO₂-C fluxes observed with the EC method. Other studies using different methods report a wider range of
aquatic CO₂ fluxes in arctic regions. These fluxes range from a CO₂-C uptake (-0.14 g m⁻² d⁻¹, Bouchard et al. (2015)) to
substantial emissions of CO₂-C (up to 2.2 g m⁻² d⁻¹, Abnizova et al. (2012)). A modeling study involving multiple lakes in
265 north-eastern European Russia found close to zero emissions (0.028 g m⁻² d⁻¹, Treat et al. (2018)). Perhaps the most striking
finding is that our estimates of aquatic CO₂ emissions are approx. 12-18 times smaller than previously reported for aquatic CO₂
emissions at the same study site (Abnizova et al., 2012). One reason for the divergent results might be the different methods
used. In Abnizova et al. (2012), the thin boundary layer model (TBL) after Liss and Slater (1974) has been used to estimate
CO₂ emissions from analyzed water samples. However, one other study found good agreement between the EC method and
270 the TBL (Eugster et al., 2003), so we cannot conclusively explain the differences.

Our approach of combining a footprint model with a land cover classification to extract fluxes from different land cover
classes allows us to determine the pond CO₂ flux. We report an uncertainty range of the pond CO₂ flux; however, we can
not identify the full uncertainty of this flux in this novel approach due to the unknown uncertainty of the footprint analysis.
Still, the pond CO₂ flux results are plausible and in the correct order of magnitude for two reasons. First, a reduced diurnal
275 variability has been observed when the pond influences the flux signal (figure 4). This indicates that the respiration rate from
the pond is lower than the respiration rate from the semi-terrestrial tundra, where ample oxygen is available in the upper soil
layer. Additionally, since the ponds have a lower vegetation density than the tundra, there is less photosynthesis. Second, when
focusing on night-time fluxes only, when only respiration occurs and no carbon uptake, there is a decrease in CO₂ emission
with an increasing weighted footprint fraction of open water (shown in figure 3), also indicating reduced decomposition in the
280 pond. Overall, the lower emissions from the pond compared to the semi-terrestrial tundra are reasonable.

4.2 CH₄ flux

We observe large differences in CH₄ emission from different wind sectors. CH₄ emissions from *Shore*_{120°} are significantly
higher than from *Shore*_{50°}, *pond* or *tundra*, independently of meteorological conditions (see section 3.3). Especially the differ-
ence between *Shore*_{120°} and *Shore*_{50°} is astounding since the shorelines share many characteristics. Both extend radially (in a
285 straight line) from the EC tower (see figure 1), thus contribute similarly to the EC flux. The underwater topography does not



Table 1. Daily mean water-atmosphere CO₂ & CH₄ fluxes from different study sites. TBL is the abbreviation for thin boundary layer model, EC for eddy covariance, CH for chamber measurement, MOD for modelled fluxes, STO for storage fluxes, and NEW for the method proposed in this study. All fluxes are given ± standard deviation, except of fluxes from this study are given as Median ^{75% Percentile} / _{25% Percentile}.

Study	Location	Period/Time	Study Site	Method	CO ₂ -C Flux (g m ⁻² d ⁻¹)	CH ₄ -C Flux (mg m ⁻² d ⁻¹)
This study	Lena Delta, Northern Siberia	11.07.- 10.09.2019	merged polygonal	EC/NEW	0.13 ^{0.24} / _{0.00}	13.38 ^{15.92} / _{10.55}
			pond	EC	-	12.96 ^{15.11} / _{10.34} – 19.18 ^{24.47} / _{14.26}
Abnizova et al. (2012)	Lena Delta, Northern Siberia	01.08. - 21.09.2008	merged polygonal			
			pond shore			
Jammet et al. (2017)	Northern Sweden	2012 - 2013	Lake Villasjön	EC	0.059	13.42 ± 1.64
Jonsson et al. (2008)	Northern Sweden	17.06. - 15.10.2005	Lake Merasjärvi	EC	0.22 ± 0.002	-
Eugster et al. (2003)	Alaska	27.07 - 31.07.1995	Toolik Lake	TBL	0.30 ± 0.01	-
				EC	0.11 ± 0.033	-
Jansen et al. (2019)	Northern Sweden	Year round, 2010 - 2017	Villasjön	TBL	0.13 ± 0.003	-
			Inre Harrsjön	CH	0.37 ± 0.060	14.04 ± 2.25
Bouchard et al. (2015)	NE Canada	July 2013 & 2014	Bylot Island, Polygonal ponds	TBL	0.22 ± 0.047	10.39 ± 1.40
			Lakes	CH	0.73 ± 0.067	13.76 ± 2.81
Sepulveda- Jauregui et al. (2015)	Alaska	June - July 2011 & 2012	8 Lakes, Yedoma	TBL & STO	-0.14 - 0.74	0.50 - 6432
			32 Lakes, Non-Yedoma	MOD	-0.085 - 0.062	0.70 - 74.5
Treat et al. (2018)	Northeast European Russia	2006 - 2015	Multiple Lakes	MOD	0.60 ± 0.58	92.86 ± 35.72
Sieczko et al. (2020)	Northern Sweden	July - August 2017	Lake Ljusvattnertjärn	CH	0.10 ± 0.10	16.80 ± 8.61
Ducharme- Riel et al. (2015)	North-East Canada	Summer 2008	15 lakes	TBL	0.028 ± 0.00011	0.84 ± 0.0
Repo et al. (2007)	Western Siberia	03.07. - 06.09.2005	MTlake	TBL	0.14 ± 0.11	-
			FTlake	TBL	0.41 ± 0.25	-
Lundin et al. (2013)	Northern Sweden	2009 (only ice-free season)	MTpond	TBL	0.44 ± 0.25	-
			27 lakes	TBL	0.18 ± 0.11	-
Kling et al. (1992)	Alaska	1975 - 1989	25 lakes	TBL	0.25 ± 0.040	5.16 ± 0.96



vary much between the two shorelines. Both shorelines have a water depth between a few centimeters and a few decimeters within meters away from the shore (see data from Boike et al. (2015a)). As previously described in section 2.1, both shorelines are dominated by *Carex aquatilis*, and from visual inspection we can not find differences in shoot density. We, therefore, assume that the vegetation type does not play a major role in explaining the differences between the CH₄ emission from *Shore*_{120°} and
290 from *Shore*_{50°}. We also examine the evolution of the shorelines at the merged polygonal pond to check whether erosion along the shoreline could drive the high CH₄ emissions. We compare a coarse image from 1965 (U.S. Geological Survey, EROS Center, 1965) with the current shoreline; yet, we can not identify signs of recent erosion. Also high resolution aerial images of the pond from 2008 (Boike et al. (2015b), resolution > 0.33 m) and 2015 (Boike et al. (2015c), resolution > 0.33 m) show no signs of erosion. Thus, we exclude erosion as a driving factor of high CH₄ emissions.

295 We also consider the possibility that local ebullition of the pond could lead to high CH₄ emissions from *Shore*_{120°}. We apply the method proposed by Iwata et al. (2018) to check for signs of ebullition events. This method uses the 20 Hz raw concentration of CH₄ to detect short-term peaks in CH₄ that originate from ebullition events. However, we can not detect ebullition events in the 20 Hz raw data.

In summary, many causes, such as meteorological conditions, vegetation type, coastal erosion, and intense ebullition events,
300 can be excluded as driving factors. Therefore, the most likely cause of the higher CH₄ emissions from *Shore*_{120°} might be a small but steady seep ebullition hot spot close to this shoreline (such as ebullition class *Kotenok* in Walter et al. (2006)). Seep ebullition hot spots have been reported to occur heterogeneously in clusters in Alaskan lakes (Walter Anthony and Anthony, 2013). So, a future visual inspection of trapped CH₄ bubbles in the ice column during wintertime, as proposed in Vonk et al. (2015), could reveal more information about the cause of the higher CH₄ emission from the *Shore*_{120°}.

305 Excluding the high emissions from *Shore*_{120°}, the CH₄ emission from the merged polygonal pond and the tundra surface have a very similar magnitude under similar meteorological conditions. In both landscape types, CH₄ is produced under anoxic conditions, but the emission pathways differ substantially. In dense soils, methane diffuses through upper soil layers and can oxidize before reaching the surface. In contrast, methane emitted in ponds can reach the surface quickly through ebullition or higher plant-mediated transport in addition to diffusion. We expected bigger differences between CH₄ emissions from the pond
310 and the tundra due to the different emission pathways. Yet, as shown in figure 6, c) and A2, we see no significant difference in CH₄ emission from the open-water areas of the merged polygonal pond and the tundra surface. Since many other ponds are smaller than the pond (making them unsuitable for studying with the EC method), and since smaller ponds tend to be stronger emitters (Holgerson and Raymond, 2016; Wik et al., 2016), our measurements might be a lower limit of overall pond-CH₄ emissions. We estimate a CH₄-C flux of $13.38 \frac{15.92}{10.55} \text{ mg m}^{-2} \text{ d}^{-1}$ (*Median* ^{75%Percentile}/_{25%Percentile}) from the merged polygonal pond
315 and $12.96 \frac{15.11}{10.34} - 19.18 \frac{24.47}{14.26} \text{ mg m}^{-2} \text{ d}^{-1}$ from the shores of this pond. This is higher than the fluxes measured by Jammet et al. (2017) from a sub-arctic lake (see also Table 1). The authors report a mean annual CH₄-C flux of $13.42 \pm 1.64 \text{ mg m}^{-2} \text{ d}^{-1}$ and a mean ice-free season CH₄-C flux of $7.58 \pm 0.69 \text{ mg m}^{-2} \text{ d}^{-1}$. A study focusing on 32 non-Yedoma thermokarst lakes in Alaska found CH₄-C emissions similar to our results ($16.80 \pm 8.61 \text{ mg m}^{-2} \text{ d}^{-1}$, Sepulveda-Jauregui et al. (2015)). Also, a synthesis of 149 thermokarst water bodies north of $\sim 50^\circ$ reports CH₄-C emissions in the same order of magnitude
320 ($27.57 \pm 14.77 \text{ mg m}^{-2} \text{ d}^{-1}$, Wik et al. (2016)). However, there is also a recent study reporting considerably lower CH₄-C



emissions of $2.95 \pm 0.75 \text{ mg m}^{-2} \text{ d}^{-1}$ in Northern Sweden (Sieczko et al., 2020) and, in contrast, a study finding CH_4 -C emissions of up to $6432 \text{ mg m}^{-2} \text{ d}^{-1}$ in North-East Canada (Bouchard et al., 2015). The wide range of waterbody methane emissions cautions us to be careful when generalizing our results even for Samoylov Island, especially since the emissions within the pond are already heterogeneous. Instead, we would like to highlight the need for more measurements of CH_4 fluxes to understand the variability of pond- CH_4 emissions better.

4.3 Upscaling the CO_2 flux

We upscale the CO_2 emissions for the island of Samoylov, the area where we have access to the high-resolution land cover classification. We find that the inclusion of pond- CO_2 emission would considerably (11%) decrease the estimate of the polygonal tundra landscape's sink function. A similar approach by Abnizova et al. (2012) found a potential increase of 35 - 62 % in the estimate of CO_2 emission from the Lena River Delta when including small ponds and lakes into the aquatic CO_2 emission. If we follow the upscaling approach by Abnizova et al. (2012) and consider overgrown water as part of the ponds, we even find a CO_2 emission reduction of 19%. Also, Kuhn et al. (2018) found waterbodies in arctic regions to be an important source of carbon, which could outbalance the tundra's sink function in a future climate. In summary, our results demonstrate that aquatic CO_2 emissions can substantially influence the carbon balance of the polygonal tundra during the growing season. We expect that the impact of ponds on the carbon balance would be even bigger when accounting for CH_4 due to the locally high emissions, and because from the pond more CH_4 gets emitted per mole of CO_2 compared to the tundra.

5 Conclusions

We find that waterbodies are a carbon source while the surrounding tundra is a carbon sink during the period July – September in agreement with prior studies (Abnizova et al., 2012; Jammet et al., 2017), even if we observe much lower aquatic CO_2 fluxes compared to previous work at the same study site (Abnizova et al., 2012). Using a novel approach to disentangle the EC fluxes from different land cover classes, we estimate that during our measurement period, the landscape CO_2 sink is reduced by 11% when including ponds rather than only considering semi-terrestrial vegetated tundra. We expect lakes to have a similar effect on the budget, though a smaller one, since lakes (a) tend to emit less greenhouse gases than ponds (Holgerson and Raymond, 2016; Wik et al., 2016) and (b) cover a similar area as ponds in our study site (Abnizova et al., 2012; Muster et al., 2012).

In contrast to the spatially more homogeneous CO_2 emissions, small-scale heterogeneity in CH_4 emissions make it difficult to find drivers of CH_4 emissions. We cannot pinpoint the drivers behind the high emissions along parts of the coastline, which might be caused by seep ebullition. Thus, we cannot estimate the impact of this heterogeneity on the landscape scale and, therefore, refrain from upscaling CH_4 emissions. Additionally, the open-water fluxes presented in this paper originate from a single merged polygonal pond since the other ponds surrounding the EC tower are too small to extract their fluxes with the footprint method applied here. So, we do not account for spatial variability of CH_4 emissions between ponds, which can be substantial (Rehder et al., 2021; Wik et al., 2016). However, we note that open-water fluxes were of a similar magnitude as the



tundra fluxes. Consequently, the main impact of ponds on the landscape CH₄ budget might be through plant-mediated transport and local ebullition.

355 While being ill-suited for very small ponds, we want to underline that the EC method is appropriate for observing greenhouse-gas fluxes from ponds with an area as small as 0.024 km². The EC method has a higher temporal resolution than the TBL method and does not disturb the exchange processes like the chamber-flux method, which eliminates the wind at the water surface. Especially when combining the EC footprint with a land cover classification, the contribution of different land cover classes can be distinguished well, and the fluxes from ponds can be studied.

360 We conclude that ponds contribute significantly to the landscape carbon budget. Changes in the Arctic hydrology and the concomitant changes in the waterbody distribution may impact the overall carbon budget of the Arctic and flip a landscape from being an overall carbon sink to becoming an overall carbon source.

Code and data availability. The data has been published at Pangaea (doi will be added as soon as it becomes available). Code can be requested from the authors.

Appendix A: Additional Figures

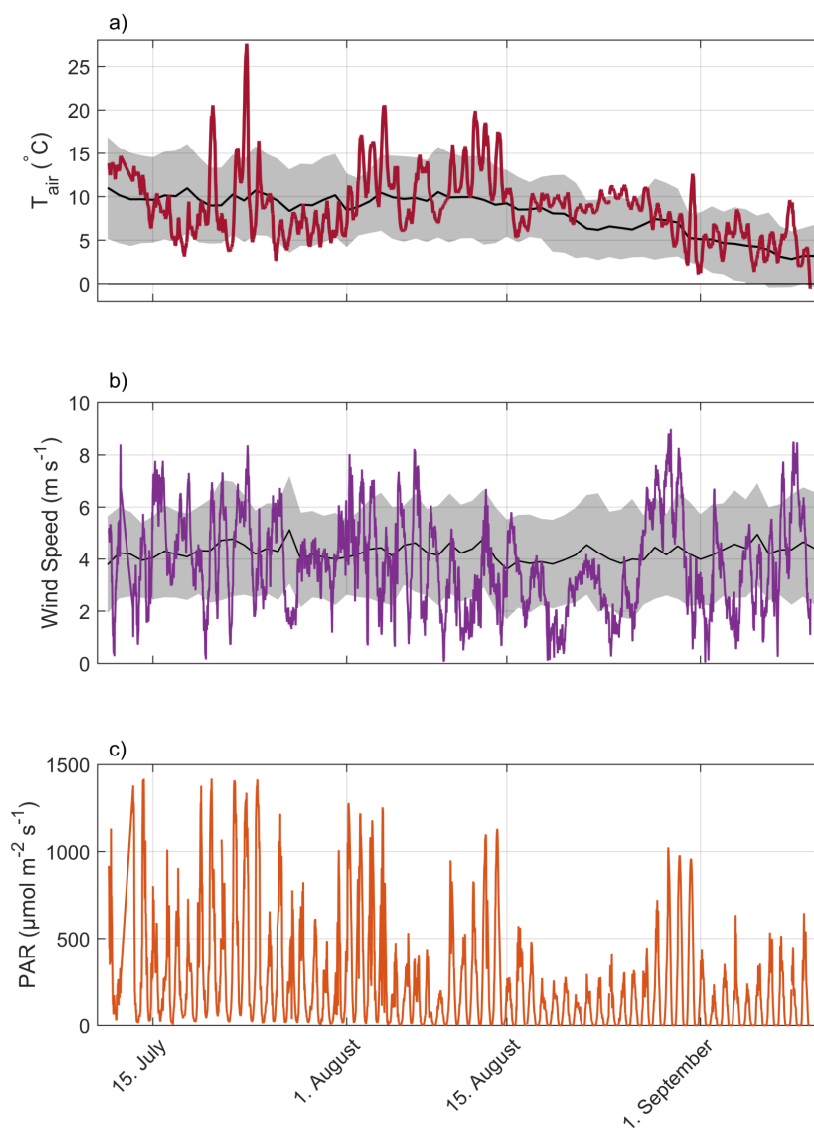


Figure A1. Time line of meteorological conditions during the observation period with air temperature in 2 meters height (a), wind speed in 3 meters height (b) and photosynthetically active radiation (PAR) (c). Mean values and standard deviation of observations during the past 16 years are plotted as black lines and gray areas.

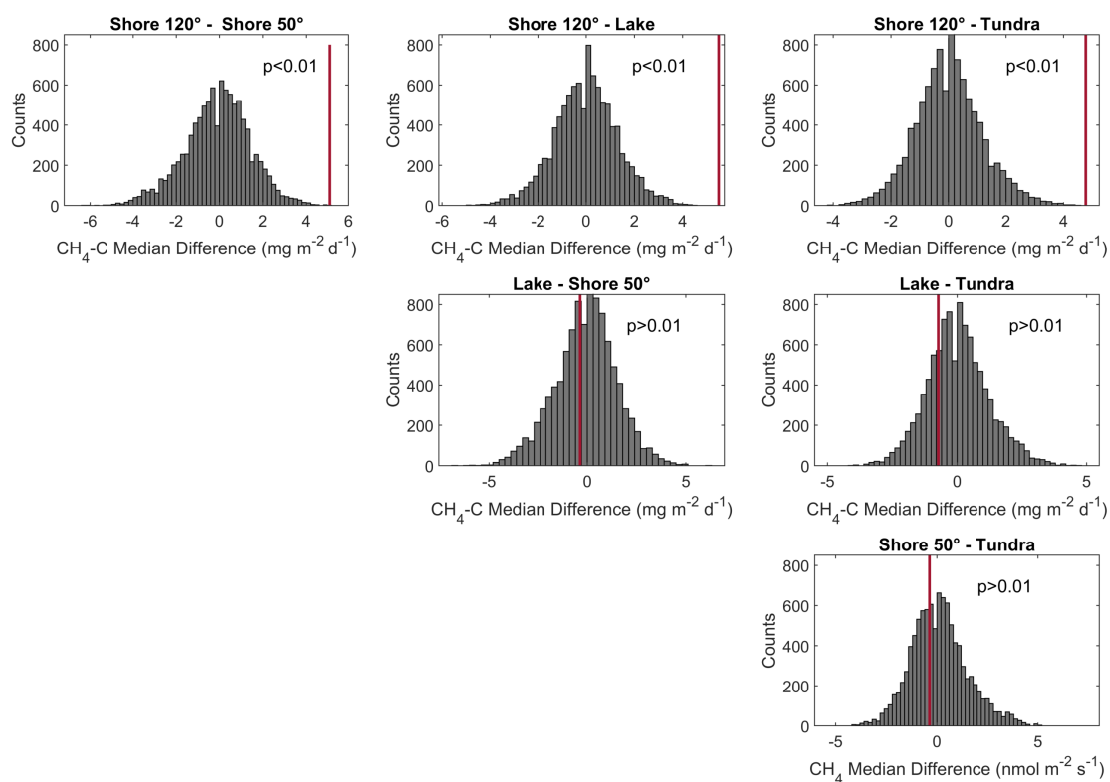


Figure A2. Histogram of permutation tests between the medians of CH₄ emissions from different wind direction classes in figure 6, b). All medians from flux observations during moderate wind speed conditions.

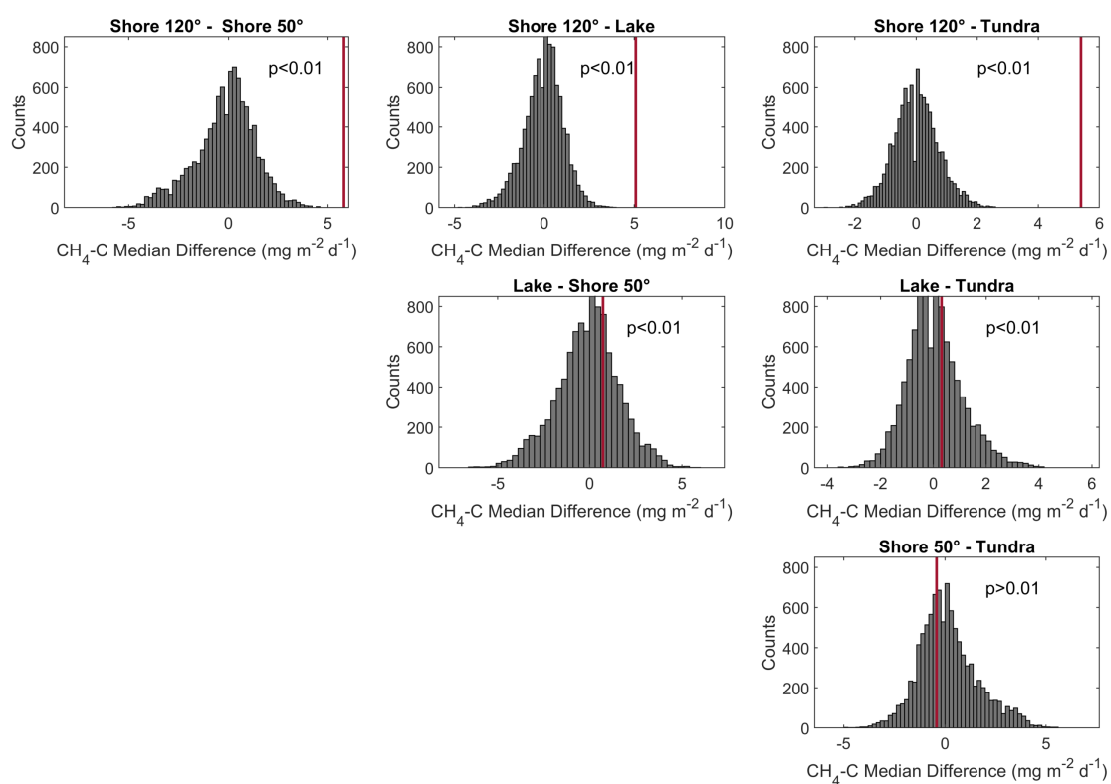


Figure A3. Histogram of permutation tests between the medians of CH₄ emissions from different wind direction classes in figure 6, c). All medians from flux observations during moderate air temperature conditions.



365 *Author contributions.* Zoé Rehder and Lars Kutzbach designed the experiments, Zoé Rehder and Lutz Beckebanze carried out the fieldwork. Zoé Rehder, Lutz Beckebanze, and Lars Kutzbach developed the idea for the analysis, and Christian Wille and Lutz Beckebanze prepared the data. The formal analysis and data visualization were performed by Lutz Beckebanze and Zoé Rehder with supervision by David Holl and Lars Kutzbach. Resources (land cover classification) have been provided by Charlotta Mirbach. Lutz Beckebanze and Zoé Rehder prepared the manuscript with contributions from all co-authors.

370 *Competing interests.* The authors declare that they have no conflict of interest.

Disclaimer. This study was funded by the Deutsche Forschungsgemeinschaft (DFG, German Research Foundation) under Germany's Excellence Strategy – EXC 2037 'CLICCS - Climate, Climatic Change, and Society' – Project Number: 390683824, contribution to the Center for Earth System Research and Sustainability (CEN) of Universität Hamburg and by the BMBF KoPf project (grant 03F0764B).

375 *Acknowledgements.* The authors thank Norman Rüggen for his tireless support before and remotely during the fieldwork, Anna Zaplavnova, Andrei Astapov, and Waldemar Schneider for their equally tireless support in the field, Andrei Astapov and Katya Abramova for additional pictures in the field, Volkmar Assmann and the station crew of Samoylov Island for their logistical support and Sarah Wiesner, Leonardo Galera, and Tim Eckhardt and for fruitful discussions during the data analysis. Also the authors thank the reviewers.



References

- Abnizova, A., Siemens, J., Langer, M., and Boike, J.: Small ponds with major impact: The relevance of ponds and lakes in permafrost
380 landscapes to carbon dioxide emissions, *Global Biogeochemical Cycles*, 26, <https://doi.org/10.1029/2011gb004237>, 2012.
- Andresen, C. G. and Lougheed, V. L.: Disappearing Arctic tundra ponds: Fine-scale analysis of surface hydrology in
drained thaw lake basins over a 65year period (1948-2013), *Journal of Geophysical Research-Biogeosciences*, 120, 466–479,
<https://doi.org/10.1002/2014jg002778>, 2015.
- Andresen, C. G., Lara, M. J., Tweedie, C. E., and Lougheed, V. L.: Rising plant-mediated methane emissions from arctic wetlands, *Global*
385 *Change Biology*, <https://doi.org/10.1111/gcb.13469>, 2017.
- Boike, J., Grüber, M., Langer, M., Piel, K., and Scheritz, M.: Orthomosaic of Samoylov Island, Lena Delta, Siberia,
<https://doi.org/10.1594/PANGAEA.786073>, <https://doi.org/10.1594/PANGAEA.786073>, 2012.
- Boike, J., Georgi, C., Kirilin, G., Muster, S., Abramova, K., Fedorova, I., Chetverova, A., Grigoriev, M. N., Bornemann, N., and Langer, M.:
Temperature, water level and bathymetry of thermokarst lakes in the continuous permafrost zone of northern Siberia - Lena River Delta,
390 Siberia, <https://doi.org/10.1594/PANGAEA.846525>, 2015a.
- Boike, J., Veh, G., Stoof, G., Grüber, M., Langer, M., and Muster, S.: Visible and near-infrared orthomosaic and orthophotos of Samoylov
Island, Siberia, summer 2008, with links to data files, <https://doi.org/10.1594/PANGAEA.847343>, 2015b.
- Boike, J., Veh, G., Viitanen, L.-K., Bornemann, N., Stoof, G., and Muster, S.: Visible and near-infrared orthomosaic of Samoylov Island,
Siberia, summer 2015 (5.3 GB), <https://doi.org/10.1594/PANGAEA.845724>, 2015c.
- 395 Boike, J., Nitzbon, J., Anders, K., Grigoriev, M. N., Bolshiyarov, D. Y., Langer, M., Lange, S., Bornemann, N., Morgenstern, A., Schreiber,
P., Wille, C., Chadburn, S., Gouttevin, I., and Kutzbach, L.: Meteorologic data at station Samoylov (2002-2018, level 2, version 201908),
link to archive, PANGAEA, <https://doi.org/10.1594/PANGAEA.905232>, 2019.
- Bouchard, F., Laurion, I., Preskienis, V., Fortier, D., Xu, X., and Whiticar, M. J.: Modern to millennium-old greenhouse gases emitted from
ponds and lakes of the Eastern Canadian Arctic (Bylot Island, Nunavut), *Biogeosciences*, 12, 7279–7298, [https://doi.org/10.5194/bg-12-](https://doi.org/10.5194/bg-12-7279-2015)
400 [7279-2015](https://doi.org/10.5194/bg-12-7279-2015), 2015.
- Bring, A., Fedorova, I., Dibike, Y., Hinzman, L., Mard, J., Mernild, S. H., Prowse, T., Semenova, O., Stuefer, S. L., and Woo, M. K.: Arctic
terrestrial hydrology: A synthesis of processes, regional effects, and research challenges, *Journal of Geophysical Research-Biogeosciences*,
121, 621–649, <https://doi.org/10.1002/2015jg003131>, 2016.
- Burba, G., Schmidt, A., Scott, R. L., Nakai, T., Kathilankal, J., Fratini, G., Hanson, C., Law, B., Mcdermitt, D. K., Eckles, R., Furtaw, M.,
405 and Velgersdyk, M.: Calculating CO₂ and H₂O eddy covariance fluxes from an enclosed gas analyzer using an instantaneous mixing ratio,
Global Change Biology, 18, 385–399, <https://doi.org/10.1111/j.1365-2486.2011.02536.x>, 2012.
- Ducharme-Riel, V., Vachon, D., del Giorgio, P. A., and Prairie, Y. T.: The Relative Contribution of Winter Under-Ice and Summer Hypolim-
netic CO₂ Accumulation to the Annual CO₂ Emissions from Northern Lakes, *Ecosystems*, 18, 547–559, [https://doi.org/10.1007/s10021-](https://doi.org/10.1007/s10021-015-9846-0)
015-9846-0, 2015.
- 410 Edgington, E. and Onghena, P.: *Randomization tests*, CRC Press, 2007.
- Eugster, W., Kling, G., Jonas, T., McFadden, J. P., Wüest, A., MacIntyre, S., and Chapin, F. S.: CO₂ exchange between air and water in
an Arctic Alaskan and midlatitude Swiss lake: Importance of convective mixing, *Journal of Geophysical Research Atmospheres*, 108,
<https://doi.org/10.1029/2002JD002653>, 2003.



- Fan, S.-M., Wofsy, S. C., Bakwin, P. S., Jacob, D. J., and Fitzjarrald, D. R.: Atmosphere-biosphere exchange of CO₂ and O₃ in the central Amazon Forest, *Journal of Geophysical Research: Atmospheres*, 95, 16 851–16 864, <https://doi.org/10.1029/JD095iD10p16851>, 1990.
- Fratini, G., Ibrom, A., Arriga, N., Burba, G., and Papale, D.: Relative humidity effects on water vapour fluxes measured with closed-path eddy-covariance systems with short sampling lines, *Agricultural and forest meteorology*, 165, 53–63, <https://doi.org/10.1016/j.agrformet.2012.05.018>, 2012.
- Gash, J. H. C. and Culf, A. D.: Applying a linear detrend to eddy correlation data in realtime, *Boundary-Layer Meteorology*, 79, 301–306, <https://doi.org/10.1007/bf00119443>, 1996.
- Holgerson, M. A. and Raymond, P. A.: Large contribution to inland water CO₂ and CH₄ emissions from very small ponds, *Nature Geoscience*, 9, 222–226, <https://doi.org/10.1038/ngeo2654>, <http://www.nature.com/articles/ngeo2654>, 2016.
- Ibrom, A., Dellwik, E., Flyvbjerg, H., Jensen, N. O., and Pilegaard, K.: Strong low-pass filtering effects on water vapour flux measurements with closed-path eddy correlation systems, *Agricultural and Forest Meteorology*, 147, 140 – 156, <https://doi.org/10.1016/j.agrformet.2007.07.007>, 2007a.
- Ibrom, A., Dellwik, E., Larsen, S. E., and Pilegaard, K.: On the use of the Webb-Pearman-Leuning theory for closed-path eddy correlation measurements, *Tellus, Series B: Chemical and Physical Meteorology*, 59, 937–946, <https://doi.org/10.1111/j.1600-0889.2007.00311.x>, 2007b.
- Iwata, H., Hirata, R., Takahashi, Y., Miyabara, Y., Itoh, M., and Iizuka, K.: Partitioning Eddy-Covariance Methane Fluxes from a Shallow Lake into Diffusive and Ebullitive Fluxes, *Boundary-Layer Meteorology*, 169, 413–428, <https://doi.org/10.1007/s10546-018-0383-1>, 2018.
- Jammet, M., Dengel, S., Kettner, E., Parmentier, F.-J. W., Wik, M., Crill, P., and Friborg, T.: Year-round CH₂ and CO₂ flux dynamics in two contrasting freshwater ecosystems of the subarctic, *Biogeosciences*, 14, 5189–5216, <https://doi.org/10.5194/bg-14-5189-2017>, 2017.
- Jansen, J., Thornton, B. F., Jammet, M. M., Wik, M., Cortés, A., Friborg, T., MacIntyre, S., and Crill, P. M.: Climate-Sensitive Controls on Large Spring Emissions of CH₄ and CO₂ From Northern Lakes, *Journal of Geophysical Research: Biogeosciences*, 124, 2379–2399, <https://doi.org/10.1029/2019JG005094>, 2019.
- Jonsson, A., Åberg, J., Lindroth, A., and Jansson, M.: Gas transfer rate and CO₂ flux between an unproductive lake and the atmosphere in northern Sweden, *Journal of Geophysical Research: Biogeosciences*, 113, 1–13, <https://doi.org/10.1029/2008JG000688>, 2008.
- Kaimal, J. C. and Finnigan, J. J.: *Atmospheric boundary layer flows: their structure and measurement*, Oxford university press, 1994.
- Kartozia, A.: Assessment of the Ice Wedge Polygon Current State by Means of UAV Imagery Analysis (Samoylov Island, the Lena Delta), *Remote Sensing*, 11, 1627, 2019.
- Kling, G. W., Kipphut, G. W., and Miller, M. C.: The flux of CO₂ and CH₄ from lakes and rivers in arctic Alaska, *Hydrobiologia*, 240, 23–36, <https://doi.org/10.1007/BF00013449>, 1992.
- Knoblauch, C., Spott, O., Evgrafova, S., Kutzbach, L., and Pfeiffer, E. M.: Regulation of methane production, oxidation, and emission by vascular plants and bryophytes in ponds of the northeast Siberian polygonal tundra, *Journal of Geophysical Research-Biogeosciences*, 120, 2525–2541, <https://doi.org/10.1002/2015jg003053>, 2015.
- Kormann, R. and Meixner, F. X.: An analytical footprint model for non-neutral stratification, *Boundary-Layer Meteorology*, 99, 207–224, 2001.
- Kuhn, M., Lundin, E. J., Giesler, R., Johansson, M., and Karlsson, J.: Emissions from thaw ponds largely offset the carbon sink of northern permafrost wetlands, *Scientific Reports*, <https://doi.org/10.1038/s41598-018-27770-x>, 2018.
- LI-COR: EddyPro Version 7.0.6, 2019.



- Liss, P. S. and Slater, P. G.: Flux of gases across the Air-Sea interface, *Nature*, 247, 181–184, <https://doi.org/10.1038/247181a0>, 1974.
- Lundin, E. J., Giesler, R., Persson, A., Thompson, M. S., and Karlsson, J.: Integrating carbon emissions from lakes and streams in a subarctic catchment, *Journal of Geophysical Research: Biogeosciences*, 118, 1200–1207, <https://doi.org/10.1002/jgrg.20092>, 2013.
- 455 MATLAB: MATLAB Software 2019b, the MathWorks, Natick, MA, USA, 2019.
- Mauder, M. and Foken, T.: Documentation and instruction manual of the eddy covariance software package TK2, Univ, Bayreuth, Abt. Mikrometeorol., ISSN, 161489166, 26–42, 2004.
- McGuire, A. D., Christensen, T. R., Hayes, D., Herault, A., Euskirchen, E., Kimball, J. S., Koven, C., Lafleur, P., Miller, P. A., Oechel, W., Peylin, P., Williams, M., and Yi, Y.: An assessment of the carbon balance of Arctic tundra: Comparisons among observations, process
460 models, and atmospheric inversions, *Biogeosciences*, 9, 3185–3204, <https://doi.org/10.5194/bg-9-3185-2012>, 2012.
- Moncrieff, J., Clement, R., Finnigan, J., and Meyers, T.: Averaging, detrending, and filtering of eddy covariance time series, in: *Handbook of micrometeorology*, pp. 7–31, Springer, 2004.
- Muster, S., Langer, M., Heim, B., Westermann, S., and Boike, J.: Subpixel heterogeneity of ice-wedge polygonal tundra: a multi-scale analysis of land cover and evapotranspiration in the Lena River Delta, Siberia, *Tellus B: Chemical and Physical Meteorology*, 64, 17 301,
465 <https://doi.org/10.3402/tellusb.v64i0.17301>, 2012.
- Muster, S., Roth, K., Langer, M., Lange, S., Cresto Aleina, F., Bartsch, A., Morgenstern, A., Grosse, G., Jones, B., Sannel, A. B. K., Sjöberg, Y., Günther, F., Andresen, C., Veremeeva, A., Lindgren, P. R., Bouchard, F., Lara, M. J., Fortier, D., Charbonneau, S., Virtanen, T. A., Hugelius, G., Palmtag, J., Siewert, M. B., Riley, W. J., Koven, C. D., and Boike, J.: PeRL: a circum-Arctic Permafrost Region Pond and Lake database, *Earth System Science Data*, 9, 317–348, <https://doi.org/10.5194/essd-9-317-2017>, 2017.
- 470 Neff, J. C. and Asner, G. P.: Dissolved organic carbon in terrestrial ecosystems: Synthesis and a model, *Ecosystems*, 4, 29–48, <https://doi.org/10.1007/s100210000058>, 2001.
- Ramsar Convention Secretariat: An introduction to the Ramsar convention on wetlands (previously The Ramsar Convention Manual), Ramsar Convention Secretariat, Gland, Switzerland, 2016.
- Rehder, Z., Zaplavnova, A., and Kutzbach, L.: Identifying drivers behind spatial variability of methane concentrations in East Siberian ponds,
475 *Frontiers in Earth Science*, 9, 183, 2021.
- Repo, M. E., Huttunen, J. T., Naumov, A. V., Chichulin, A. V., Lapshina, E. D., Bleuten, W., and Martikainen, P. J.: Release of CO₂ and CH₄ from small wetland lakes in western Siberia, *Tellus, Series B: Chemical and Physical Meteorology*, 59, 788–796, <https://doi.org/10.1111/j.1600-0889.2007.00301.x>, 2007.
- Runkle, B. R., Sachs, T., Wille, C., Pfeiffer, E. M., and Kutzbach, L.: Bulk partitioning the growing season net ecosystem exchange of CO₂
480 in Siberian tundra reveals the seasonality of its carbon sequestration strength, *Biogeosciences*, 10, 1337–1349, <https://doi.org/10.5194/bg-10-1337-2013>, 2013.
- Sepulveda-Jauregui, A., Walter Anthony, K. M., Martinez-Cruz, K., Greene, S., and Thalasso, F.: Methane and carbon dioxide emissions from 40 lakes along a north-south latitudinal transect in Alaska, *Biogeosciences*, 12, 3197–3223, <https://doi.org/10.5194/bg-12-3197-2015>, 2015.
- 485 Siczko, A. K., Duc, N. T., Schenk, J., Pajala, G., Rudberg, D., Sawakuchi, H. O., and Bastviken, D.: Diel variability of methane emissions from lakes, *Proceedings of the National Academy of Sciences*, 117, 21 488–21 494, <https://doi.org/10.1073/pnas.2006024117>, <https://www.pnas.org/content/117/35/21488>, 2020.



- Squires, M. M. and Lesack, L. F.: The relation between sediment nutrient content and macrophyte biomass and community structure along a water transparency gradient among lakes of the Mackenzie Delta, *Canadian Journal of Fisheries and Aquatic Sciences*, 60, 333–343, <https://doi.org/10.1139/f03-027>, 2003.
- 490 Treat, C. C., Marushchak, M. E., Voigt, C., Zhang, Y., Tan, Z., Zhuang, Q., Virtanen, T. A., Räsänen, A., Biasi, C., Hugelius, G., Kaverin, D., Miller, P. A., Stendel, M., Romanovsky, V., Rivkin, F., Martikainen, P. J., and Shurpali, N. J.: Tundra landscape heterogeneity, not interannual variability, controls the decadal regional carbon balance in the Western Russian Arctic, *Global Change Biology*, 24, 5188–5204, <https://doi.org/10.1111/gcb.14421>, 2018.
- 495 U.S. Geological Survey, EROS Center: CORONA Satellite Photographs, 1965.
- Vickers, D. and Mahrt, L.: Quality control and flux sampling problems for tower and aircraft data, *Journal of Atmospheric and Oceanic Technology*, 14, 512–526, [https://doi.org/10.1175/1520-0426\(1997\)014<0512:QCAFSP>2.0.CO;2](https://doi.org/10.1175/1520-0426(1997)014<0512:QCAFSP>2.0.CO;2), 1997.
- Vonk, J. E., Tank, S. E., Bowden, W. B., Laurion, I., Vincent, W. F., Alekseychik, P., Amyot, M., Billet, M. F., Canário, J., Cory, R. M., Deshpande, B. N., Helbig, M., Jammet, M., Karlsson, J., Larouche, J., Macmillan, G., Rautio, M., Walter Anthony, K. M., and
500 Wickland, K. P.: Reviews and syntheses: Effects of permafrost thaw on Arctic aquatic ecosystems, *Biogeosciences*, 12, 7129–7167, <https://doi.org/10.5194/bg-12-7129-2015>, 2015.
- Walter, K. M., Zimov, S. A., Chanton, J. P., Verbyla, D., and Chapin, F. S.: Methane bubbling from Siberian thaw lakes as a positive feedback to climate warming, *Nature*, 443, 71–75, <https://doi.org/10.1038/nature05040>, 2006.
- Walter Anthony, K. M. and Anthony, P.: Constraining spatial variability of methane ebullition seeps in thermokarst lakes using point process
505 models, *Journal of Geophysical Research: Biogeosciences*, 118, 1015–1034, <https://doi.org/10.1002/jgrg.20087>, 2013.
- Webb, E. K., Pearman, G. I., and Leuning, R.: Correction of flux measurements for density effects due to heat and water vapour transfer, *Quarterly Journal of the Royal Meteorological Society*, 106, 85–100, <https://doi.org/10.1002/qj.49710644707>, 1980.
- Wik, M., Varner, R. K., Anthony, K. W., MacIntyre, S., and Bastviken, D.: Climate-sensitive northern lakes and ponds are critical components of methane release, *Nature Geoscience*, 9, 99–105, <https://doi.org/10.1038/ngeo2578>, 2016.